Supporting Information

Carbon Microtube Array with Multihole Cross Profile: Releasing the Stress and Boosting Long-Cycling and High-Rate Potassium Ion Storage

Bo Wang,[a] Fei Yuan,[a] Wei (Alex) Wang,[b,*] Di Zhang,[a,*] Huilan Sun,[a] Kai Xi,[c] Dianlong Wang,[a] Jianhua Chu,[d] Qiujun Wang,[a] and Wen Li[a]

[a] School of Materials Science and Engineering, Hebei University of Science and Technology, Shijiazhuang, 050018, China

[b] Beijing Key Laboratory of Bio-inspired Energy Materials and Devices, School of Space and Environment, Beihang University, Beijing, 100191 PR China

[c] Department of Materials Science and Metallurgy, University of Cambridge, Cambridge CB3 0FS, UK

[d] State Key Laboratory of Advanced Metallurgy, University of Science and Technology Beijing, Beijing 100083, China

*Corresponding authors.

E-mail addresses: wwangbj@pku.edu.cn (W. W), snowfoxzd@hebust.edu.cn (D. Z)

Experimental Section

Synthesis of CQDs: The CQDs were prepared by a simple hydrothermal reaction. First, 2 g of fresh sycamore leaves and 40 mL of distilled water were placed in a 50 ml L Teflon-lined autoclave and heated in a 200 °C dry box for 8 h, and cooled to room temperature for washing, drying and grinding.

Hydrothermal carbonization (HTC) has arisen as a powerful and sustainable technology for the synthesis of nano-structured carbon materials. During the hydrothermal carbonization of biomass or biomass precursors, first the cellulose is hydrolyzed into glucose and further dehydrated to 5-hydroxyme-thylfurfural (HMF) and levulinic acid. The process continues by a cascade of chemical reactions involving mainly Diels–Alder cycloadditions and ring-opening reactions.[1] During this step, small nucleation clusters are formed through nucleation reactions. As the reaction time increases, the nucleation clusters grow into nanoscale carbon particles. Several groups have reported the use of hydrothermal carbonization of biomass to produce CQDs, which are the nucleation clusters forming prior to the growth into the final nanoscale sized carbon particle materials.[2, 3]

Synthesis of PCM: Appropriate amount of CQD_S were placed in a tube sintering furnace for 3 h at 850 °C under argon atmosphere and then cooled to room temperature naturally. The same method was used to synthesize the products of 0.5 h, 1.5 h, 6 h.

Details of finite element model simulation: We set up a series of three-dimensional finite element models, using the general modeling software Hypermesh to model the structure of three rods (solid rods, hollow tubes, hollow tubes with multihole cross profile). The analysis was performed in Abaqus, a finite element analysis software, and normal displacement was applied on the surface of the models to expand the volume by 100 % to simulate the stress caused by ion insertion.

There are no specific constraint boundary conditions for the calculation of the three bars, so the calculation is analyzed by the method of inertial release. According to the requirements, each rod is analyzed with carbon material (elastic modulus 10 Gpa, pine ratio 0.13, density 1.38 g cm^{-3}), so the following describes the application of load.

1、Solid rod: normal displacement is applied to the outer surface of the solid rod; displacement is applied axially;

2、Hollow tube: normal displacement is applied to the inner and outer surfaces of the hollow tube; axial displacement is applied;

3、Hollow tubes with multihole cross profile: normal displacement is applied to the inside and outside of the hollow tubes with multihole cross profile; axial displacement is applied.

Since the expansion ratio of the total volume is 100%, it means that the volume is expanded by one V. Therefore, the radial and axial expansions are taken as 0.5V, respectively. The calculation of the diameter and length after expansion has the following requirements.

1 First, all three models expand in the radial direction. And, assuming the length of the solid rod is constant.

2 The inner diameters(id) of the hollow tube and hollow tubes with multihole cross profile are expanded according to the expansion ratio of the respective outer diameters(od).

3 The calculation result is the analytical value obtained by iterating in 3D software rather than purely numerical calculations.

Based on these, a brief description of the calculation process is given in Table S1.

Table S1. Related calculations for finite element simulation analysis

<table>
<tr><th rowspan="2">Model</th><th colspan="3">Initial state</th><th colspan="3">After expansion</th></tr>
<tr><th colspan="2">R
(μm)</th><th>H
(μm)</th><th>V
(μm^3)</th><th>R_1
(μm)</th><th>H_1
(μm)</th><th>V_1
(μm^3)</th></tr>
<tr><td>Solid rod</td><td colspan="2">3.5</td><td>10</td><td>$\pi R^2H/4$</td><td>$0.5V + V = \pi HR_1^2/4$
R_1=4.28</td><td>$0.5V = \pi h_1 R_1^2/4$
h_1=3.33
H_1=H+ h_1=13.3</td><td>2V</td></tr>
<tr><td rowspan="2">Hollow tube</td><td>R_{od}</td><td>3.5</td><td rowspan="2">10</td><td rowspan="2">$H(\pi R_{od}^2 - \pi R_{id}^2)/4$</td><td>$R_{1od}$=$R_1$=4.28</td><td rowspan="2">$0.5V = h_1(\pi R_{1od}^2 - \pi R$
h_1=4
H_1=H+ h_1=14</td><td rowspan="2">2V</td></tr>
<tr><td>R_{id}</td><td>2.3</td><td>R_{1id}=R_{id}*R_{1od}/R_{od}
(R_{1id} =2.81)</td></tr>
<tr><td rowspan="2">Hollow tubes with multihole cross profile</td><td>R_{od}</td><td>3.5</td><td rowspan="2">10</td><td rowspan="2">$H(\pi R_{od}^2 - \pi R_{id}^2)/4$</td><td>$R_{1od}$=$R_1$=4.28</td><td rowspan="2">$0.5V = h_1(\pi R_{1od}^2 - \pi R$
h_1=4
H_1=H+ h_1=14</td><td rowspan="2">2V</td></tr>
<tr><td>R_{id}</td><td>2.3</td><td>R_{1id}=R_{id}*R_{1od}/R_{od}
(R_{1id} =2.81)</td></tr>
</table>

The pure numerical calculation in table S1 is only a general process for determining the length and diameter after expansion. The specific calculation is carried out by three-dimensional software. The results are as follows:

1 Solid stick: original: diameter: 3.5 μm, length: 10 μm;

After expansion: diameter: 4.27 μm, length: 11.42 μm.

2 Hollow tubes: original: outer diameter: 3.5 μm, inner diameter: 2.3 μm, length: 10 μm;

After expansion: outer diameter: 4.27 μm, inner diameter: 2.8 μm, length: 11.39 μm.

3 Hollow tube with multiholes cross profile: original: outer diameter: 3.5 μm, inner diameter 2.3 μm, length: 10 μm;

After expansion: outer diameter: 4.27 μm, inner diameter: 2.81 μm, length: 11.35 μm.

Materials Characterizations: The morphologies structures were researched by scanning electron microscopy (SEM, Hitachi SU8010), transmission electron microscopy (TEM, JEOL JEM-2010). The physical structures were examined by XRD (Bruker D2 Phaser X-Ray Diffractometer with Cu Kα radiation), the structural component of the product was also done via X-ray photoelectron spectroscopy (XPS, ESCALAB 250 Xi). Surface functional groups were studied using a Nicolet-10X15XFourier transform infrared spectrometer (FT-IR). The thermal analysis was carried out under N_2 atmosphere by using thermogravimetric (Rigaku Thermo plus TG 8120) methods. The specific surface area, pore diameter distribution, and cumulative pore volume were measured on a TriStar II 3020 instrument (Micromeritics Instrument Corporation, USA), calculated from the N_2 adsorption–desorption isotherms.

Electrochemical Measurements: The working electrodes were composed of the as-obtained active material, acetylene black (AB), and polyvinylidene fluoride(PVDF) with a mass ratio of 7:2:1. The slurry was cast onto the copper foil and dried at 80 °C under vacuum for 10 h. Circular electrodes with a diameter of 10 mm were obtained using a punch machine.The specific capacity is calculated based on the mass of active material. Coin cells (CR2032) were assembled with potassium foil as the counter/reference electrode, a glass-fiber separator, and 0.8 M KPF6 in EC:DEC (1:1) with 3vol. % of fluoroethylene carbonate (FEC) as an electrolyte in argon-filled glove

box. The galvanostatic tests of cycle and rate performance were tested by multi-channel land battery test system (LAND-CT2001A) in the fixed voltage window from 0.01 V to 2.5 V versus K^+/K at room temperature. Cyclic voltammetry (CV) was conducted by a CHI618D electrochemical workstation with scan rate 0.1 mV s^{-1}. Electrochemical impedance spectroscopy (EIS) was measured on a CHI 660D electrochemical workstation over the frequency range from 0.01 to 10^5 Hz (amplification voltage: 5 mV).

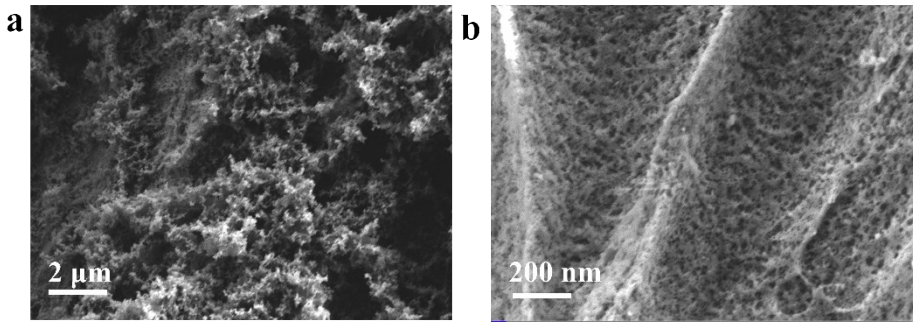

Figure S1. SEM images of the CQD_S.

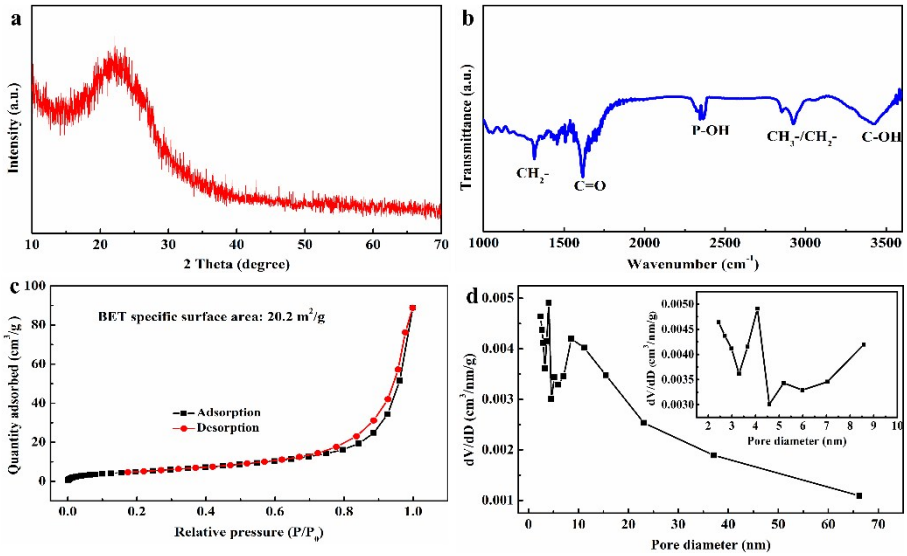

Figure S2. Physical characterization of CQD_S. a) XRD pattern, b) FTIR spectra, c) nitrogen adsorption–desorption isotherms and d) pore size distribution.

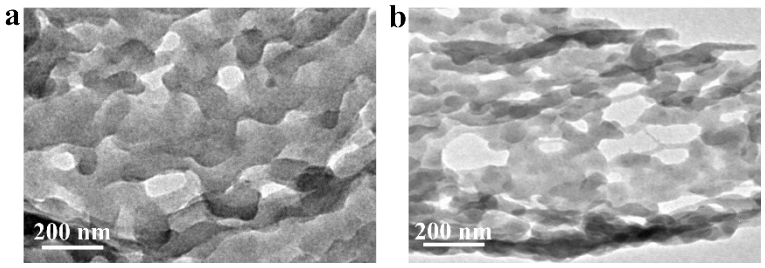

Figure S3. TEM images of the of PCM.

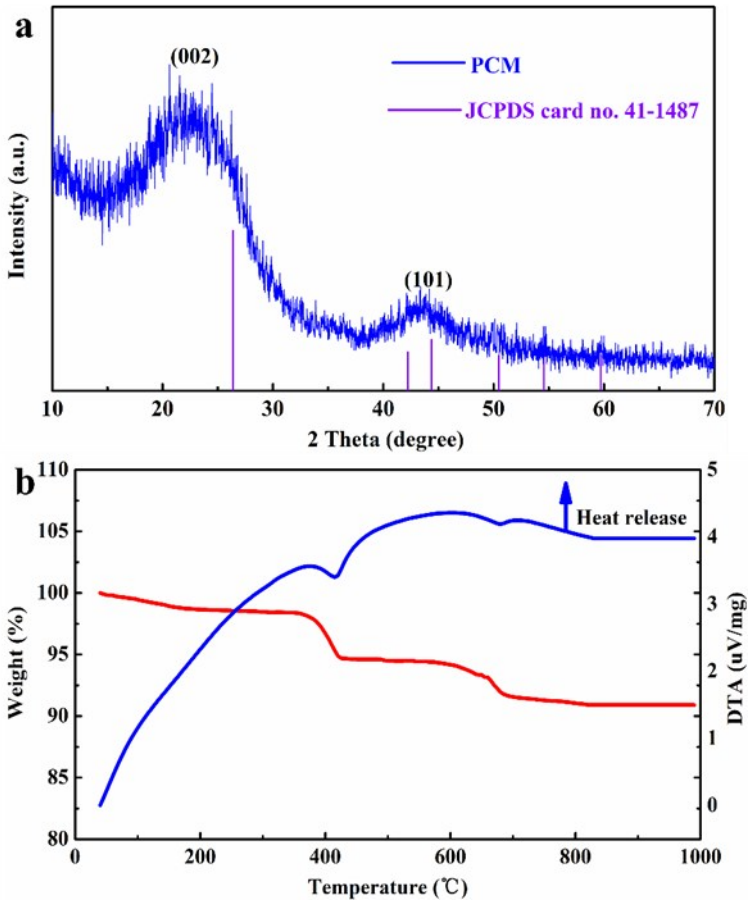

Figure S4. a) XRD of PCM and b) TG curves of CQD_S.

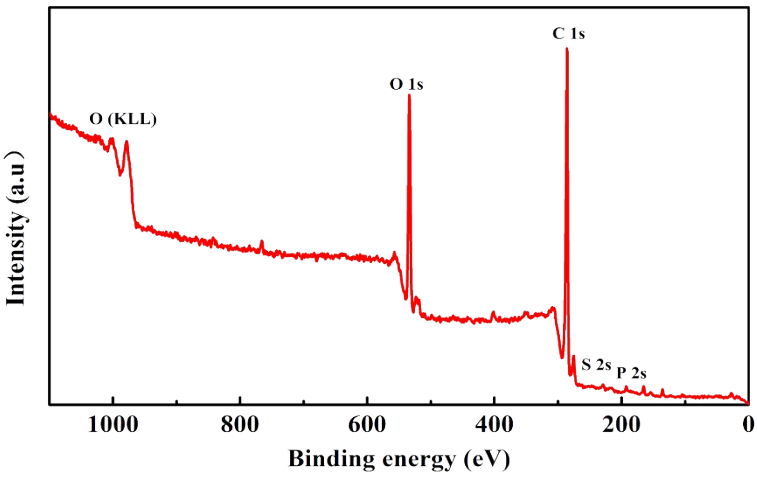

Figure S5. XPS survey spectrum of PCM.

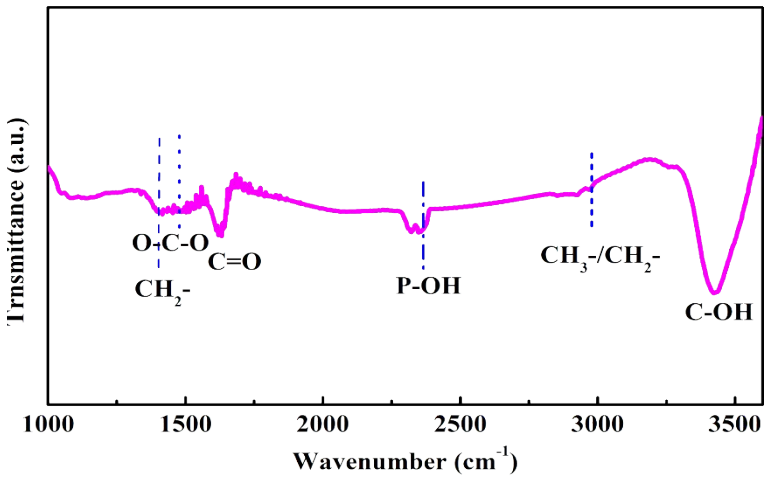

Figure S6. FTIR spectra of PCM.

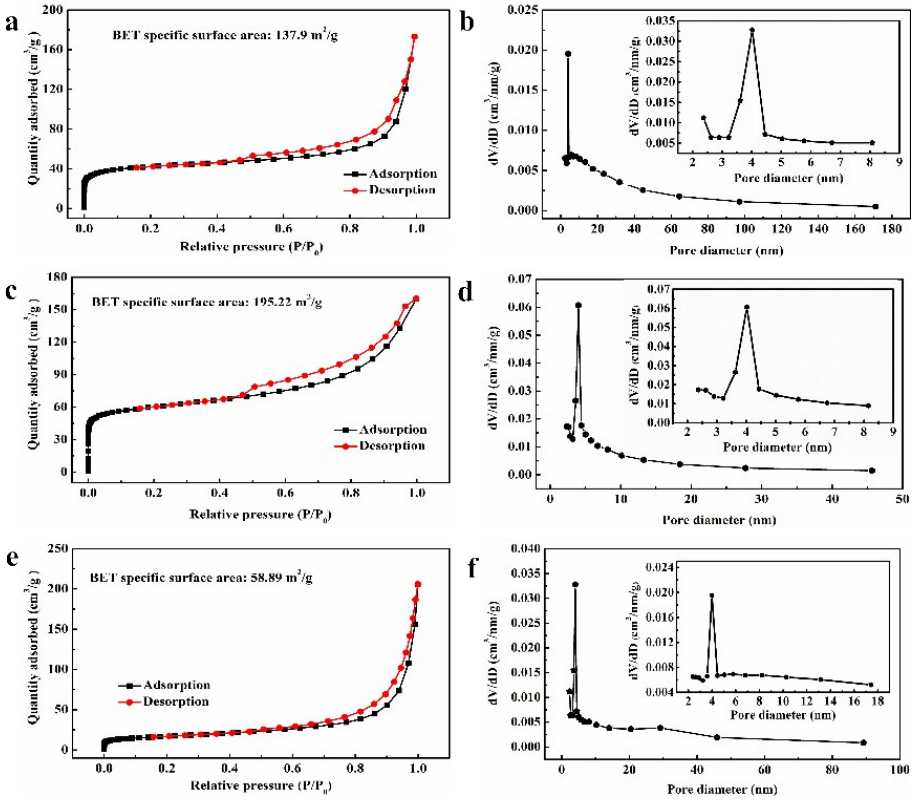

Figure S7. Nitrogen adsorption–desorption isotherms and pore size distribution of products calcined for different times at 850 °C under Ar atmosphere. a, b) 0.5 h, c, d) 1.5 h, e, f) 6 h.

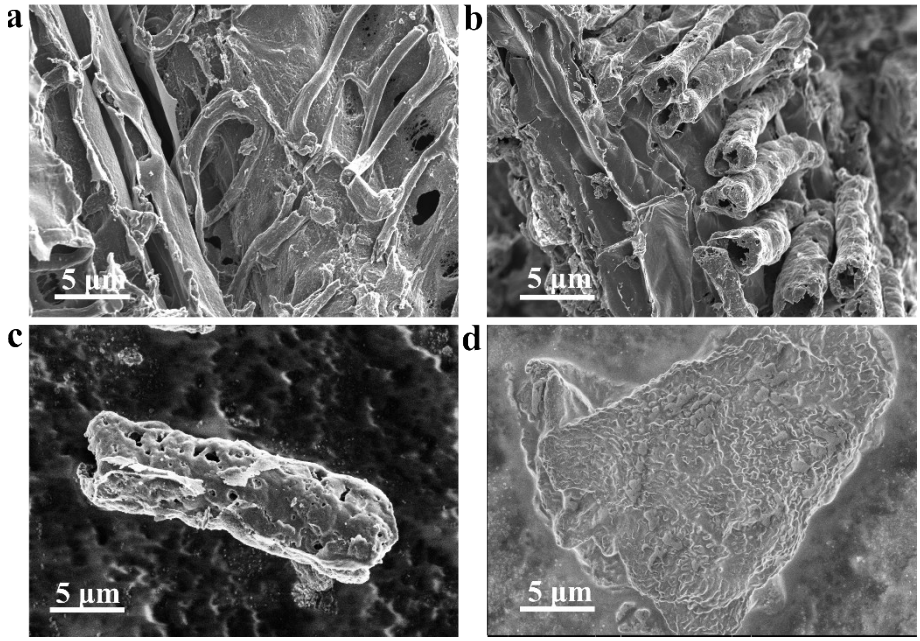

Figure S8. Morphology of samples with different carbonization times under Ar atmosphere at 850 °C. a) 0.5 h, b) 1.5 h, c) 3 h, d) 6 h.

In the obtained hydrothermal product, a precursor of a porous oxygen-enriched structure was formed, which then generated the instantaneous high internal pressure during subsequent high-temperature rapid pyrolysis.[4] Under Na catalysis, the abundant carbon atoms produced from the decomposition of the hydrothermal product self-assembled to form carbon tube. Due to the presence of high internal pressure, which can effectively restrain the stack deposition of carbon network during the spontaneous expansion process of carbon lamellar layer and the successful formation of the carbon tube is ensured.[4] The existence of abundant carbon bonds may be favorable for the formation of carbon tube.[4]

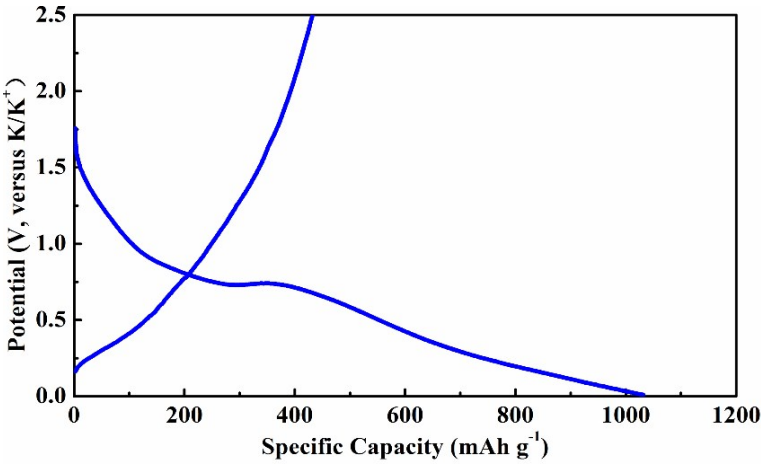

Figure S9. The initial charge and discharge profiles of PCM at 500 mA g^{-1}.

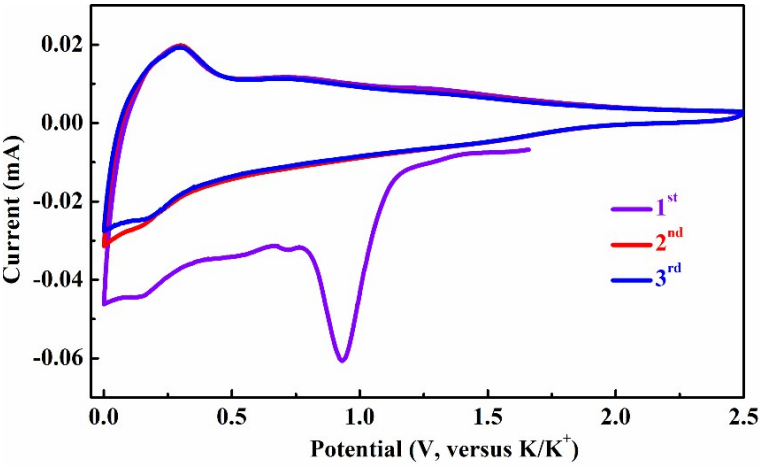

Figure S10. CV profiles of PCM at a scan rate of 0.1 mV s^{-1} between 0.01 and 2.5 V (*versus* K^+/ K).

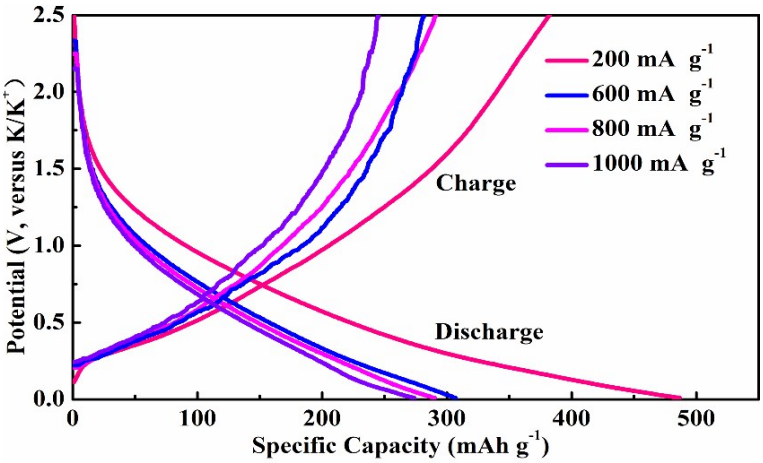

Figure S11. The second charge and discharge profiles of PCM at various current density of 200, 600, 800 and 1000 mA g^{-1}.

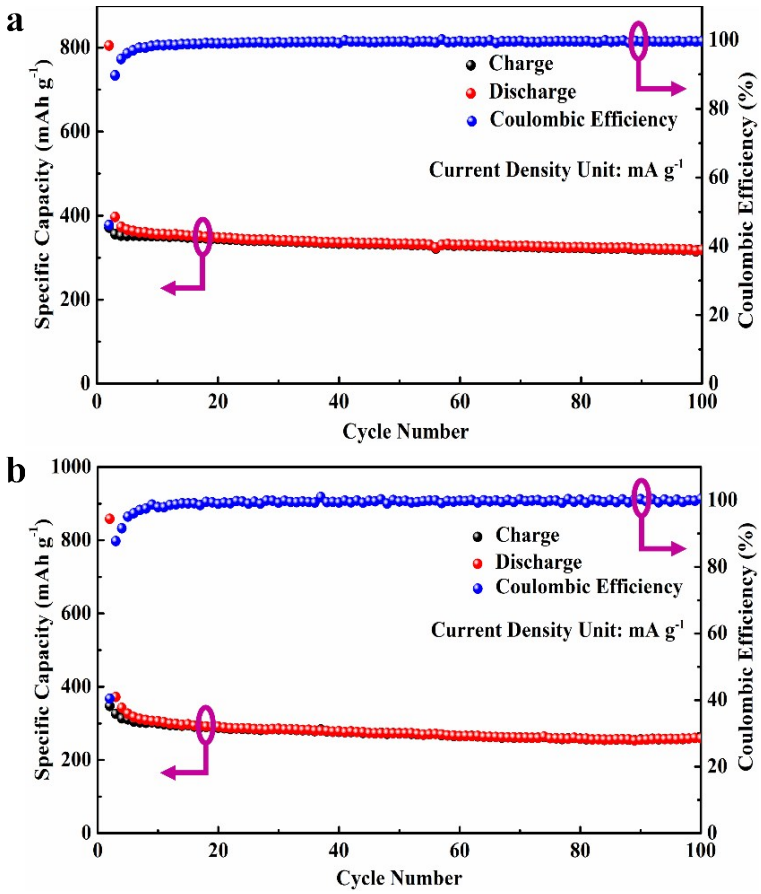

Figure S12. The cycle performance of PCM at (a) 800 and (b) 1000 mA g^{-1} over 100 cycles with a Coulomb efficiency close to 100 %.

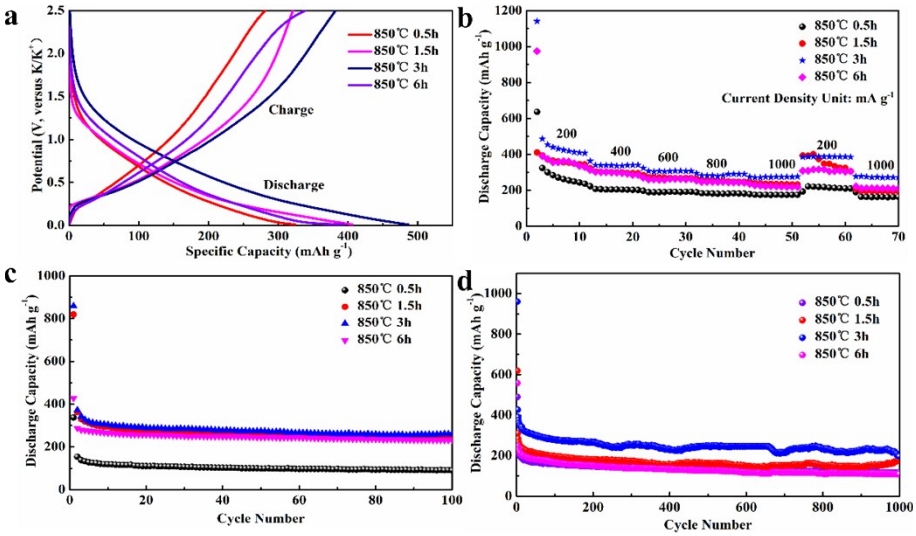

Figure S13. Comparison of electrochemical performance of samples with different carbonization times under Ar atmosphere at 850 °C. a) The second charge and discharge profiles at 200 mA g^{-1}. b) Rate capability at varied current densities from 200 to 1000 mA g^{-1}. c) Cycle performance at a high current densities of 1000 mA g^{-1} for 100 cycles. d) Long-term cycling stability over 1000 cycles at 2000 mA g^{-1}.

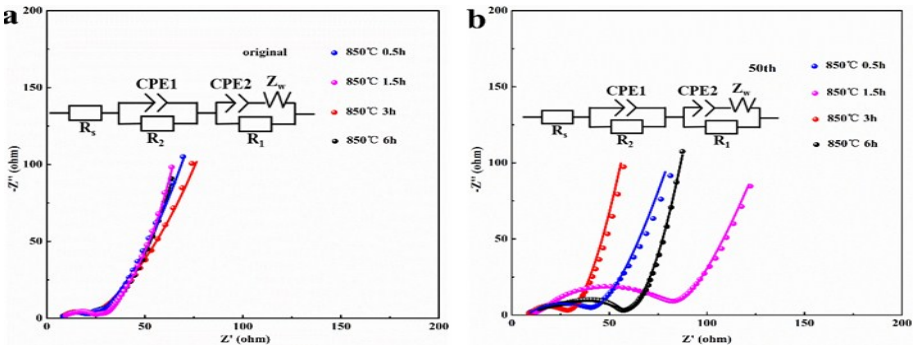

Figure S14. Nyquist plots of EIS for the sample with the different carbonization times under Ar atmosphere at 850 °C. a) Initial state and b) after 50 cycles at a current density 1000 mA g^{-1}.

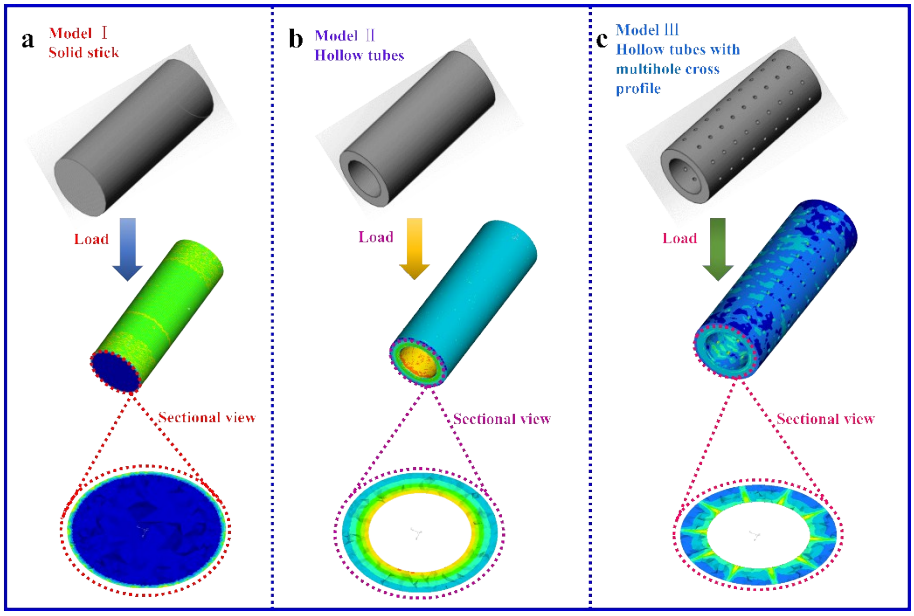

Figure S15. Simulation of differential models structural stability suffer from diffusion-induced stresses. Drawing standard size models with Solidworks and calculated stress distributions overall view and radial section view of a) solid stick, b) hollow tube and c) hollow tubes with multihole cross profile.

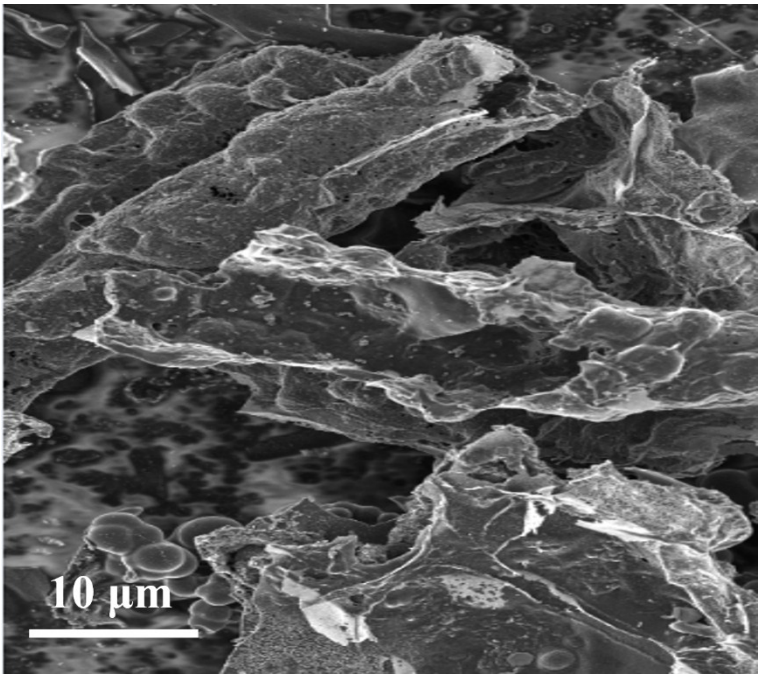

Figure S16. SEM images of PCM electrode over 2000 cycles at 2000 mA g^{-1}.

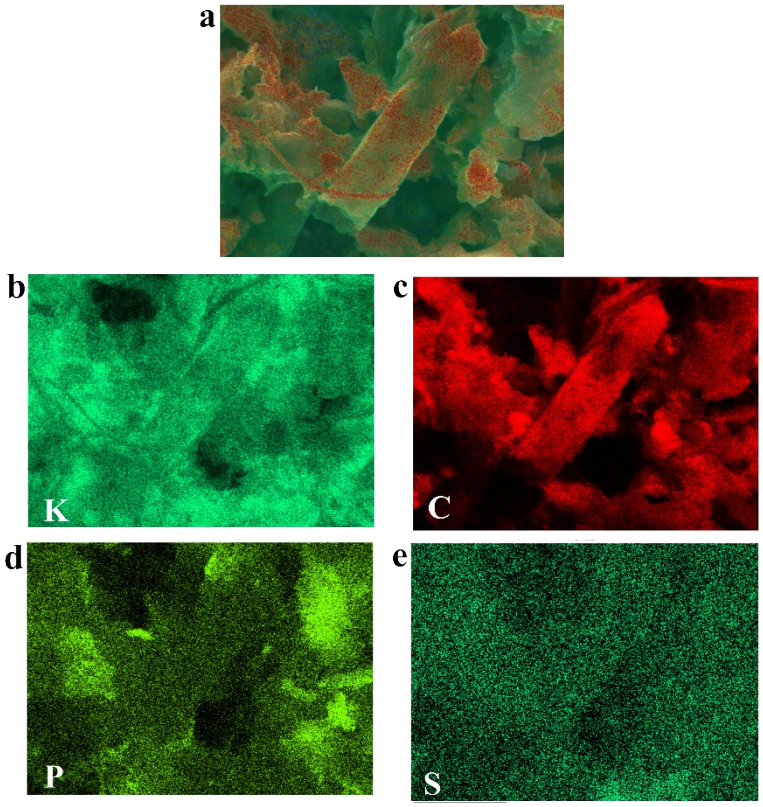

Figure S17. a) EDS image and the corresponding elemental mappings of b) K, c) C, d) P and e) S in PCM electrode after fully discharged to 0.01 V.

(For better imaging, the cycled electrode material is thoroughly washed with dimethyl carbonate for 5 times and then dried for 8 h at 80 °C under vacuum atmosphere.)

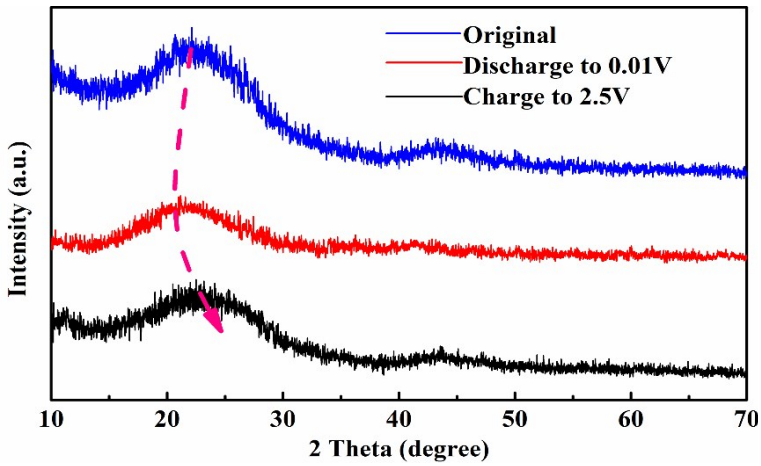

Figure S18. XRD patterns of PCM electrode at original state, full discharge state and full charge state.

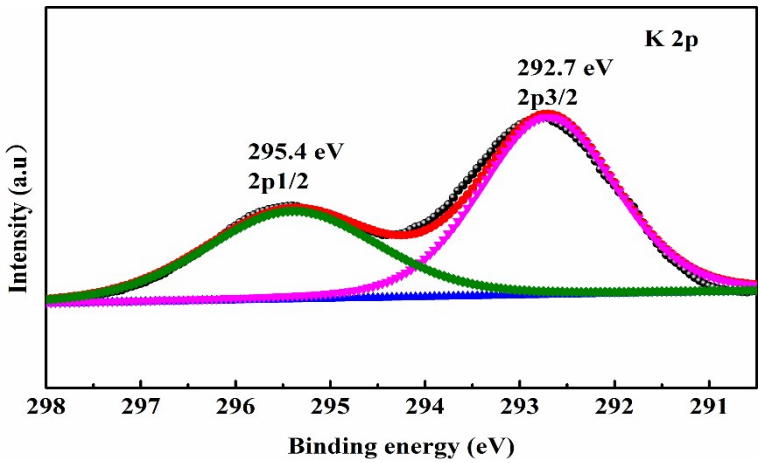

Figure S19. High-resolution K 2p XPS patterns of PCM electrode after fully discharged to 0.01 V.

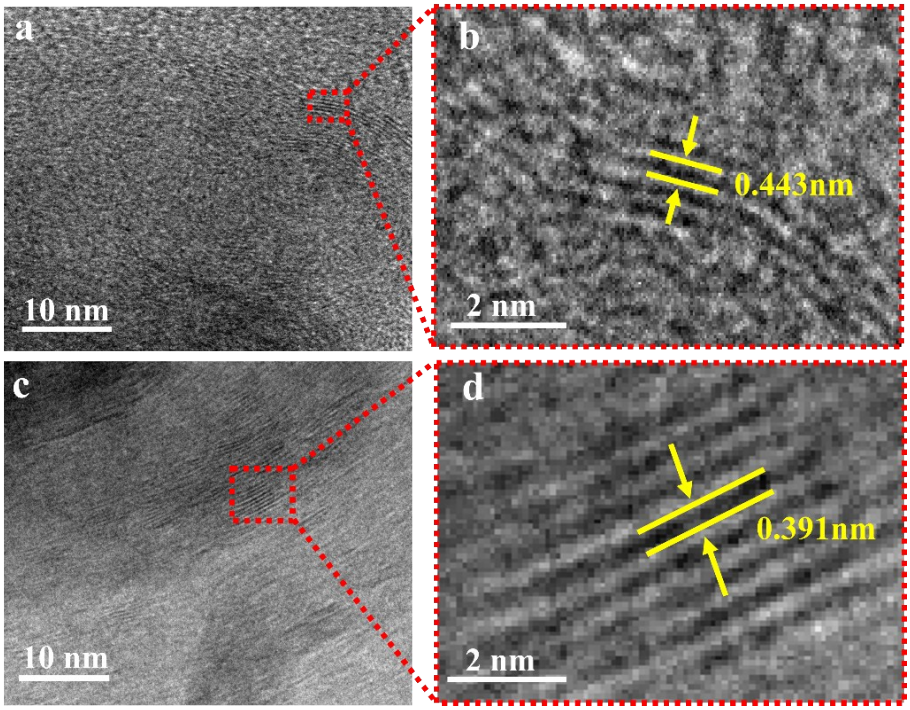

Figure S20. HRTEM image of PCM electrode after (a, b) fully discharged to 0.01 V and (c, d) fully charged to 2.5 V.

Table S2. The element content of PCM via XRF analysis

Element	Wt%	Atomic %
C	92.92	94.99
O	6.63	4.78
Na	0.06	0.03
S	0.17	0.07
P	0.22	0.09
Total	100.00	100.00

Table S3. Comparison of carbon-based anodes in potassium-ion batteries

Material name	Cycle number	Specific capacity	Reference
PCM	**2000**	**177.6 mAh g^{-1} at 10C**	**This work**
	100	**394.7 mAh g^{-1} at 2.5C**	
Carbon Nanofibers	20	80 mAh g^{-1} at 0.25C	Ref. 5
Hard carbon	100	136 mAh g^{-1} at 5C	Ref. 6
Hard/Soft Carbon	200	180 mAh g^{-1} at 1C	Ref. 7
Carbon Nanocage	100	212 mAh g^{-1} at 0.1C	Ref. 8
Graphite (KS4)	200	246 mAh g^{-1} at 0.1C	Ref. 9
N-doped Graphite	100	300 mAh g^{-1} at 0.5C	Ref. 10
N-doped Carbon	180	200 mAh g^{-1} at 2.5C	Ref. 11
Graphitic carbon	1000	80 mAh g^{-1} at 50C	Ref. 12
P/O-doped Graphene	600	160 mAh g^{-1} at 10C	Ref. 13
N/O-doped carbon	1100	120 mAh g^{-1} at 5.25C	Ref. 14
Polynanocrystalline Graphite	300	14 mAh g^{-1} at 5C	Ref. 15
N/O-rich carbon fiber	1900	110 mAh g^{-1} at 10C	Ref. 16
Few layered graphe	100	150 mAh g^{-1} at 0.5C	Ref. 17
Ordered mesoporous carbon	1000	146.5 mAh g^{-1} at 5C	Ref. 18

Table S4. The element content of PCM electrode after fully discharged to 0.01 V via EDS analysis

Element	Wt%	Atomic %
C	48.76	64.14
O	22.4	24.49
P	1.19	0.62
S	0.21	0.11
K	**25.72**	**10.64**
Total	100.00	100.00

References

1 N. Baccile, G. Laurent, F. Babonneau, F. Fayon, M. M. Titirici and M. Antonietti, J. Phys. Chem. C, 2009, **113**, 9644–9654.

2 Z. L. Wu, P. Zhang, M. X. Gao, C. F. Liu, W. Wang, F. Leng and C. Z.Huang, J. Mater. Chem. B, 2013, **1**, 2868–2873.

3 Z. C. Yang, M. Wang, A. M. Yong, S. Y. Wong, X. H. Zhang, H.Tan, A. Y. Chang, X. Li and J. Wang, Chem. Commun. 2011, **47**,11615–11617.

4 H. Cui, J. Zheng, P. Yang, Y. Zhu, Z. Wang and Z.Zhu , ACS Appl. Mater.Interfaces, 2015, **7**, 11230-11238.

5 Y. Liu, F. Fan, J. Wang, Y. Liu, H. Chen, Y. Xuz and C. Wang, *Nano Lett*s, 2014, **14**, 3445-3452.

6 Z. Jian, Z. Xing, C. Bommier, Z. Li and X. J. Ji, *Adv. Energy Mater.*, 2016, **6**, 1501874.

7 Z. Jian, S. Hwang, Z. Li, A. S. Hernandez, X. Wang, Z. Xing, D. Su and X. Ji, *Adv. Funct. Mater.*, 2017, **27**, 1700324.

8 B. Cao, Q. Zhang, H. Liu, B. Xu, S. Zhang, X. Chen and H. Song, *Adv. Energy Mater.*, 2017, **8**, 1801149.

9 Z. Jin, X. Zou, Y. Zhu, Y. Xu and C. J. Wang, *Adv. Funct. Mater.*, 2016, **26**, 8103-8110.

10 K. Share, A. P. Cohn, R. Carter, B. Rogers and C. L. Pint, *ACS Nano*, 2016, **10**, 9738-9744.

11 Y. Xie, Y. Chen, L. Liu, P. Tao, M. Fan, N. Xu, X. Shen and C. Yan, *Adv. Mater.*, 2017, **29**, 1702268.

12 A. P. Cohn, N. Muralidharan, R. Carter, K. Share, L. Oakes and C. L. Pint, *J. Mater. Chem. A*, 2016, **4**, 14954-14959.

13 Y. Huang, L. Ke, J. Liu, Z. Xing, X. Duan, I. Shakir and Y. J. Xu, *J. Mater. Chem. A*, 2017, **5**, 2710-2716.

14 J. Yang, Z. Ju, Y. Jiang, Z. Xing, B. Xi, J. Feng and S. Xiong, *Adv. Mater.*, 2018, **30**, 1700104.

15 Z. Xing, Y. Qi, Z. Jian and X. J. Ji, *ACS Appl. Mater. Interfaces*, 2017, **9**, 4343-4350.

16 R. A. Adams, J. M. Syu, Y. Zhao, C. T. Lo, A. V. Varma and G. Pol, *ACS Appl. Mater. Interfaces*,, 2017, **9**, 17872-17879.

17 K. Share, A. P. Cohn, R. E. Carter and C. L. Pint, *Nanoscale*, 2016, **8**, 16435-16439.

18 W. Wang, J. Zhou, Z. Wang, L. Zhao, P. Li, Y. Yang, C. Yang, H. Huang and S. Guo, *Adv. Energy Mater.*, 2018, **8**, 1701648.